

THE DINOSAUR IN THE DETAIL: HIGH ORDER HARMONICS IN THE LIGHT CURVES OF ECCENTRIC PLANETARY SYSTEMS

ZEPHYR PENOYRE AND EMILY SANDFORD

Department of Astronomy, Columbia University, New York, NY 10025

ABSTRACT

Eccentric planets cause higher-order harmonics in the photometric power spectra of their host stars. This is true for the light curves of stars displaying the out-of-transit effects of tidal distortion, relativistic beaming, and reflections from the planetary surface. Taking this into account is both useful and important for understanding stellar power spectra, since even planets with eccentricities typical of our solar system can excite harmonics which cannot be explained by circular-orbit models. We present an analysis of these signals, including publicly available code for computation of theoretical out-of-transit light curves, `OoT`. Finally, we discuss prospects for current and future observations.

Keywords: planets and satellites: detection, stars: oscillations, stars: planetary systems, methods: analytical, methods: statistical

1. INTRODUCTION

Power spectra measure the strength of oscillations of a given frequency in a time-dependent signal. In the context of planet detection, the time evolution of the apparent luminosity of a star (the light curve) can have various periodicities that hint at the presence of an orbiting planet. The power spectrum of a light curve reveals such periodicities.

The best-studied type of periodic signal in a light curve due to a planet is a planetary transit, during which a planet crosses our line of sight to its host star, blocking some starlight during a narrow phase window every orbit (see e.g. Henry et al. 1999; Charbonneau et al. 2000). However, we only observe transits of planets whose orbits are inclined nearly edge-on to our line-of-sight, which comprise a small fraction of all planetary systems.

In this paper, we instead focus on three *out-of-transit* effects which cause periodic photometric variability in stars:

- Tides - Tidal distortions of the stellar surface due to the planet's gravitational influence (often called ellipsoidal variations in the literature; Morris 1985).
- Beaming - The relativistic aberration of the star's light due to its motion as it orbits around the barycenter of the star-planet system (Loeb & Gaudi 2003).
- Reflection - Redirection of some small fraction of the star's light towards the observer via reflection

off the planet's atmosphere/surface (see e.g. Charbonneau et al. 1999).

We focus on these three effects because a) all three signals should be present in every planetary system (though they may be vanishingly small) and b) they are well constrained: simple theoretical models can be constructed to model each with few free parameters and assumptions about the planet or the star.

For planets on circular orbits, we would expect tides to modulate the starlight twice per orbit. The distorted star is approximately lemon-shaped, with bulges pointing towards and away from the planet. Thus the star appears to grow smaller and larger in cross-section (and therefore dimmer and brighter, respectively) with a frequency twice that of the planet's orbital frequency.

Beaming will lead to a photometric variation with the same frequency as the planet's orbit; the star grows brighter as it moves towards us and darker as it retreats.

Reflection should also cause a signal with approximately the same frequency as the planet's orbit. The reflection signal is dimmest when the planet is between the observer and the star (when no reflected light reaches us) and brighter as it moves behind the star.

However, as we showed in Penoyre & Stone (2018) (PS18), limiting our analysis of the above effects to planets on circular orbits can drastically underestimate the magnitude of their photometric signal and its utility in discovering planets. PS18 specifically focused on tides over an eccentric orbit, providing a simple analytic description of their observable effects and showing that they can be visible regardless of viewing angle and are

rich in information about the planet and the star.

Photometric signals due to tides, beaming, and reflection are most visible for massive planets on orbits passing close to their host star (well within Mercury’s distance from the Sun). Perhaps surprisingly with reference to our own solar system, many such planets have been discovered (Winn & Fabrycky 2015), enough to deserve the moniker “hot-Jupiter,” which we will use as a shorthand.

Eccentric hot-Jupiters, too, are in no short supply (Kane et al. 2012). The extreme nature of these systems suggests that they might be short-lived, since close-in planets are expected to tidally circularise over (cosmologically) short periods (Matsumura et al. 2008). Whilst these eccentric hot-Jupiters present puzzles for theories of the formation (see e.g. Lin et al. 1996; Batygin et al. 2016), evolution (Triaud et al. 2010) and dynamics (Naoz et al. 2011) of planetary systems, we will show that their properties give us great opportunities for their detection and characterisation.

We will also show that a pervasive quirk of the analysis of planetary power spectra, oscillations at 3 times the planetary orbital frequency (Esteves et al. 2013; Armstrong & Rein 2015; Cowan et al. 2017), is a natural consequence of eccentric planetary orbits.

2. PHOTOMETRIC EFFECTS OF TIDES, BEAMING, AND REFLECTIONS

Throughout this work, we are primarily concerned with the fractional change in luminosity of a star, as a function of time, due to the presence of a planetary companion. We will start by summarising the effects of tides, beaming, and reflections on a star’s light curve.

We shall not discuss transits (eclipses of a star by an orbiting planet), though they too have non-trivial power spectra, as they are already well understood (see e.g. Seager & Mallén-Ornelas 2003), and only a small fraction of planets will have sufficiently fortuitous alignments for an eclipse to be visible. Even in systems with visible transits, the below analysis can be performed on the rest of the light curve (i.e., the light curve once the transit signal has been fit and divided out), and more properties of the system can be derived, or tighter constraints placed on those derived from the transit.

Let us define the fractional change in luminosity

$$\delta = \frac{\Delta L}{L}, \quad (1)$$

where L is the luminosity the star would have in the absence of a companion, and ΔL is the apparent change in this luminosity. We will frequently make use of the subscripts t , b , r , and Σ to specify the tidal, beaming, reflection, and total effects respectively.

Here, we consider a planet with mass M_p and radius

R_p on an orbit with semi-major axis a and eccentricity e around a star with mass M (assumed to be $\gg M_p$) and radius R .

The orbit obeys

$$r(t) = \frac{a(1 - e^2)}{(1 + e \cos \Phi)} = a(1 - e \cos \eta), \quad (2)$$

where r is the orbital radius and $\Phi(t)$ is the angle, relative to the star, between the planet’s position at periape and its position at time t (often called the true anomaly). $\eta(t)$ is a useful simplification satisfying

$$\sqrt{1 - e} \tan \frac{\eta}{2} = \sqrt{1 + e} \tan \frac{\Phi}{2}. \quad (3)$$

$\eta(t)$ can also be found (numerically) from

$$t(\eta) = \sqrt{\frac{a^3}{GM}}(\eta - e \sin \eta), \quad (4)$$

and thus the position of the planet can be found at any given t (Binney & Tremaine 2008).

From this we can read off the period

$$T = 2\pi \sqrt{\frac{a^3}{GM}} \quad (5)$$

and the planet’s orbital frequency

$$\omega_p = \frac{2\pi}{T} = \sqrt{\frac{GM}{a^3}}. \quad (6)$$

All of the signals discussed in this paper will be composed of oscillations with a frequency equal to integer multiples of ω_p . We shall often make use of the shorthand of saying such a signal of frequency ω is at the n^{th} harmonic, where $\omega = n\omega_p$.

We will work in spherical co-ordinates with polar angle θ (ranging from 0 at the north pole, to π at the south pole) and azimuthal angle ϕ ranging from 0 to 2π . We orientate the system such that the planet orbits in the equatorial plane ($\theta = \frac{\pi}{2}$) and $\phi = 0$ points towards the position of the planet’s periape. It will be convenient to define a second azimuthal angle, relative to the planet’s position at time t ,

$$\psi(t, \phi) = \phi - \Phi(t). \quad (7)$$

The observed light curve and power spectrum depend on the orientation of the system relative to the observer. Let the observer be situated at some angle (θ_v, ϕ_v) , where $\theta_v = 0$ is equivalent to viewing the system from the top, or face-on, and $\theta_v = \frac{\pi}{2}$ corresponds to an edge-on view (in which transits would be visible). It will again be convenient to define a second azimuthal viewing angle, relative to the planet’s position:

$$\psi_v(t) = \phi_v - \Phi(t). \quad (8)$$

With these co-ordinates in hand, we can calculate δ for tides, beaming, and reflections.

2.1. Tides

Following the derivation in PS18, for a non-rotating star tidally distorted by a small perturber, the deviations to the stellar radius at the surface can be described by

$$\frac{\Delta R(t, \theta, \phi)}{R} = \beta \frac{M_p}{M} \left(\frac{R}{r(t)} \right)^3 \frac{3 \sin^2 \theta \cos^2(\psi(t, \phi)) - 1}{2} \quad (9)$$

where β is a dimensionless constant describing the response of the star to tides. For simplicity we take the result for a stellar surface that follows the equipotential, $\beta = 1$.

The tidal distortions described by Equation 9 affect the light curve in two ways: (i) by changing the apparent area of the star and (ii) by changing the gravitational force (and hence the pressure, temperature and flux) at the surface. The total photometric change, integrated over the stellar surface visible from (θ_v, ϕ_v) , can be shown analytically to be

$$\delta_t(t, \theta_v, \phi_v) = -\frac{13}{16} \frac{M_p}{M} \left(\frac{R}{r} \right)^3 (3 \sin^2 \theta_v \cos^2 \psi_v - 1) \quad (10)$$

(PS18, section 3.2). Here we have used the Eddington limb darkening law,

$$\frac{I(\mathbf{r})}{I_0} = \frac{2}{5} \left(1 + \frac{3}{2} (\hat{\mathbf{r}} \cdot \hat{\mathbf{l}}) \right) \quad (11)$$

where I is the intensity at some point \mathbf{r} on the surface of the star, \mathbf{l} is the line of sight direction (hats denote unit vectors), and I_0 is the intensity at the projected centre. This law gives a good general fit to most systems and is sufficiently accurate for calculations integrating over the whole area of the star.

2.2. Beaming

Loeb & Gaudi (2003) give a simple expression relating the velocity of a star to its fractional change in luminosity due to relativistic beaming, neglecting the spectral dependence of the emission:

$$\delta_b = \frac{4v_l}{c}. \quad (12)$$

c here is the speed of light, and v_l is the projection of the star's orbital velocity along the line of sight. Assuming $M_p \ll M$, v_l is equal to

$$v_l(t, \theta_v, \phi_v) = v_p \frac{M_p}{M} \sin \theta_v (\sin(\psi_v(t)) + e \sin \phi_v), \quad (13)$$

where v_p is the velocity of the planet at periapease,

$$v_p = \sqrt{\frac{GM}{a(1-e^2)}} \quad (14)$$

(Lovis & Fischer 2010).

Thus we find

$$\delta_b(t, \theta_v, \phi_v) = \frac{4}{c} \sqrt{\frac{GM}{a(1-e^2)}} \frac{M_p}{M} \sin \theta_v (\sin \psi_v + e \sin \phi_v). \quad (15)$$

2.3. Reflection

Of the processes considered in this work, the reflection of a star's light by an orbiting planet requires the largest degree of approximation. The fraction of the light incident on the planet which is reflected (the albedo) depends greatly on the properties of the planet's atmosphere or surface. The chemical composition, thermodynamic properties, and even the weather systems in a planetary atmosphere can affect the amount of light reflected, especially as a function of angle (see e.g. Jansen & Kipping 2017; Cowan & Agol 2011).

Here we will use one of the simplest relevant models: a perfectly scattering surface (often called a Lambert surface/sphere) which absorbs radiation and re-emits some fraction of it isotropically.

In this model, an infinitesimal surface element absorbs energy at a rate proportional to the flux from the star and the apparent surface area of the element (taking into account inclination). It then radiates some fraction, A_b (the Bond albedo), of this energy out uniformly over a solid angle of 2π .

This gives an observed apparent luminosity that satisfies

$$\delta_r(t, \theta_v, \phi_v) = A_g \left(\frac{R_p}{r} \right)^2 (\sin \gamma + (\pi - \gamma) \cos \gamma) \quad (16)$$

where γ is the angle between the line of sight and the direction from which the planet is illuminated. Thus $0 < \gamma < \pi$ and $\cos \gamma = -\sin \theta_v \cos \psi_v$. A_g is the geometric albedo, and is equal to $\frac{2}{3} A_b$ for a Lambert sphere. (See Seager 2010 for a more detailed derivation of these results.)

We do not consider thermal radiation from the planet, i.e. energy from the star re-radiated by the planet at its equilibrium temperature. As even the closest planets have equilibrium temperatures of $\sim 1000\text{K}$ or below, the contribution to the light curve when viewed in wavelengths close to optical light (as is true for the *Kepler* and TESS surveys) will be small.

3. LIGHT CURVES AND POWER SPECTRA

Let us consider an example planet, with mass $M_p = 3M_j$ (Jupiter masses), radius $R_p = \frac{3}{2}R_j$ (Jupiter radii), and geometric albedo $A_g = 0.15$, on an orbit with semi-major axis $a = 0.1\text{AU}$ and eccentricity $e = 0.25$. Let it be the companion of a Sun-like star (stellar mass $M = M_\odot$ and radius $R = R_\odot$). These properties have been chosen so as to make the contribution of tides, beaming

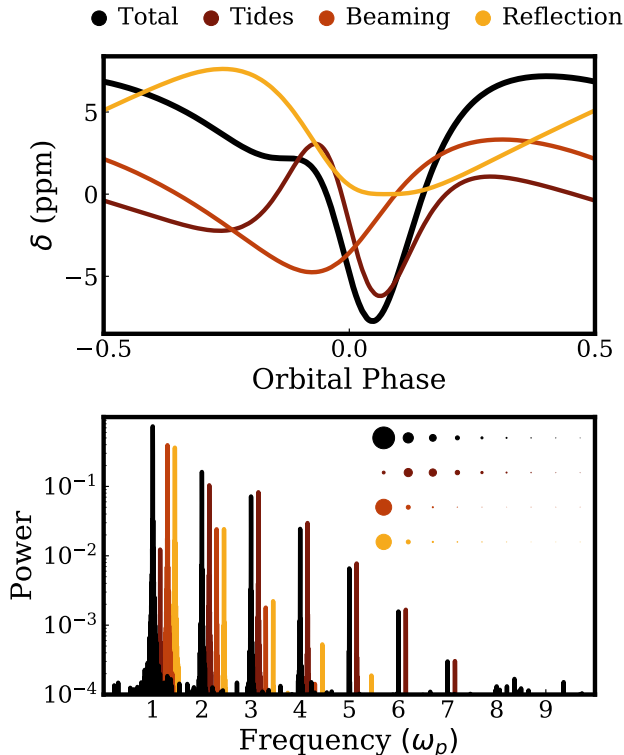


Figure 1. The light curve (top) and power spectrum (bottom) caused by a planet with $M_p = 3M_j$ and $R_p = \frac{3}{2}R_j$ on an orbit with $a = 0.1AU$ and $e = 0.25$ around a sun-like star ($M = M_\odot, R = R_\odot$). The period of this planet is roughly 10 days, and we have set the orbital phase equal to 0 at the moment of periape. The photometric contribution is shown individually for tidal distortions of the star (dark red), relativistic beaming caused by the star’s motion (brick red) and reflections of the star’s light by the planet (yellow), and the sum of these effects is shown in black. The power spectrum is computed for each individual signal over 100,000 data points and is normalised relative to the total signal. The power spectra have been shifted to make each visible (but all fall at integer multiples of ω_p in reality). The circles shown in top right give a simple visual representation of the power in each harmonic, with area proportional to power. The system is viewed from an angle in the equatorial plane of the orbit ($\theta_v = \frac{\pi}{2}$, $\phi_v = \frac{\pi}{4}$).

and reflections approximately equal in magnitude, and we will use this example planet throughout.

In PS18, we showed that such a planet is well within the distribution of confirmed exoplanets, and many systems exist which should show significantly larger photometric variation.

For any planet, the values of δ are small ($\ll 1$), due to the mass and radius of a planet being a fraction of that of a star. Thus the effects of tides, beaming, and reflection are independent and additive, so we can find each separately and add them to yield

$$\delta_\Sigma = \delta_t + \delta_b + \delta_r. \quad (17)$$

Computing the power spectrum of these photometric variations is a more nuanced task, and so we fall back

upon established tools and methods. For all power spectra shown here, we use the `LombScargle` function from the `astropy` package, which implements the methods of Press & Rybicki (1989); see VanderPlas 2017 for a full summary.

There is always a fear of artificially injecting a periodic signal into data through its processing. To avoid that in this work, we calculate δ at random points in time over an irrational multiple of the planet’s orbital period. Unless otherwise specified, 10,000 data points are used, over an observational baseline of roughly 100 orbital periods.

Figure 1 shows the light curve, and the power spectrum, of our example planet (viewed edge-on, $\theta_v = \frac{\pi}{2}$, with $\phi_v = \frac{\pi}{4}$). The profiles have been calculated via `OoT`, a publicly available code that we are releasing alongside this work (see Appendix A). The independent contributions of tides, beaming, and reflections are shown, as well as the total signal.

Looking first at the light curve, we see that the tidal, beaming, and reflection signals are all markedly different, and while each is approximately sinusoidal, the combined signal is not. At some phases, the three add together to yield a large peak, whereas at others they cancel.

A perceptive reader may notice that only the beaming signal is centred around $\delta = 0$. Reflections can only add to the observed luminosity of the star: some fraction of the light that would otherwise be radiated away is instead redirected to the observer. The tidal signal can be centred around positive or negative δ depending on viewing angle.

Moving to the power spectrum, we see not only the familiar peaks at ω_p and $2\omega_p$ (which are expected even for planets on circular orbits; see section 1), but also many peaks of similar amplitude reaching up to high harmonics. The peaks are discrete, and the power spectrum appears not as a continuous function but as a series of Dirac delta functions, and thus the spectrum could be well represented by a Fourier series expansion.

The individual power spectra of the tidal, beaming, and reflection signals are also shown, and we can see that all three show some power in the 3rd harmonic and higher. The dominant contribution to the beaming and tidal signatures is still at the planet’s orbital frequency, with the beaming signal falling off quickly at higher frequencies and the reflection signal falling off more slowly and extending to higher harmonics.

It is the tidal signal that resembles the titular stegosaurus¹: a series of spikes that rises to a crest at

¹ It has been argued that these spines more resemble a Dimetrodon skeleton, but unfortunately that isn’t a true dinosaur,

some harmonic and then drops off as a long tail. For this example planet, the dominant contribution is still at the second harmonic (as expected for the circular-orbit case), though as we will show, this is not true for high eccentricities. There is also some contribution from tides at the planet’s orbital frequency.

3.1. The role of viewing angle and eccentricity

Moving to a wider array of possible system parameters, Figure 2 shows similar light curves and power spectra for the same planet-star system, but now with varying eccentricity and viewing angle (defined in Table 1).

Examining first the light curves in Figure 2, we see that for $e = 0$, each signal is well-represented by a sinusoid (perfectly so for tides and beaming). As we move to higher eccentricity, the signals develop richer features, the tidal signature comes to dominate, and the majority of the variation is now centred around the short window when the planet is near periape. For approximately circular orbits, the signal drops off as the observer moves out of the orbital plane (through oblique to face-on projections); however, as shown in PS18, for eccentric systems, the variation in luminosity is almost equally visible from all angles (with both tides and, to a smaller extent, reflections being visible in perfectly face-on systems).

The power spectra in Figure 2 encompass a lot of detail, so we shall go through them piece by piece. Here, we have expressed the spectra in terms of the signal amplitude

$$A(\omega) = 2\sqrt{\frac{P(\omega)}{N}} \quad (18)$$

where $P(\omega)$ is the power and N the number of data points. For sharply peaked spectra such as these, this is equivalent to the magnitude of the coefficients of the Fourier series representation of $\delta(t)$. Thus we can directly relate the amplitude of the power spectra to that of the light curves.

For planets on circular orbits, we see that the power spectrum is independent of ϕ_v , and only the total amplitude depends on θ_v (this is not true at higher eccentricities). We also see that the reflection signal, even for circular orbits, is not perfectly represented by a single sinusoid, with some small contribution at the second harmonic (which might otherwise be mistaken for a small tidal signal).

For small eccentricities, roughly equivalent to those of planets in our own solar system ($0.01 < e < 0.2$), we start to see higher-order harmonics.

As we move to larger eccentricities, the amplitude of higher-order harmonics, particularly those associated

	Edge-on		Oblique	Face-on
	Periapse-Aligned	Periapse-Misaligned		
θ_v	$\frac{\pi}{2}$	$\frac{\pi}{2}$	$\frac{\pi}{3}$	0
ϕ_v	0	$\frac{\pi}{2}$	$\frac{\pi}{4}$	0

Table 1. The viewing angles used in Figure 2. The sketches show the orbit of an eccentric system, with each line-of-sight shown as a thick red line. For the oblique angle the projection is directly out of the page.

with tides, increases. Visible signal in the power spectrum appears for the face-on case; however, even though it is dominated by tides, its highest peak falls at ω_p . Only for these higher eccentricities does the dependence on the azimuthal viewing angle, ϕ_v , become easily visible.

Note that the characteristic amplitude of individual peaks does not vary greatly. For highly eccentric systems, with significantly larger δ , it is not the characteristic amplitude of the peaks but the number of harmonics that yields a larger signal in the light curve.

3.2. The dinosaur in the detail

Figure 3 represents visually the relative strength of power spectrum peaks at the first few harmonics as a function of eccentricity.

In this figure, we can see clearly that tidal signatures peak at higher and higher harmonics as eccentricity increases (yielding those characteristic “stegosaurus spines”). For $e > 0.5$, the spectrum is spread over so many peaks as to make the relative power almost invisible in these plots, though the total power summed over all harmonics increases rapidly for increasing eccentricity.

The beaming and reflection signatures have a strong peak at the 1st harmonic, with more power in higher harmonics for larger e . At any chosen eccentricity, the signal from reflection has significantly more power in higher harmonics than the beaming signal.

Let us take a moment here to build some intuition as to where these higher-order harmonics originate from.

As detailed in the introduction, simple intuition can be applied to the circular case. Let us apply similarly simple intuition to the near-radial case ($e \rightarrow 1$). As the eccentricity approaches unity, any signal will occur over a shorter time window as the time the planet spends near periape decreases. Thus, in the limit of extreme eccentricities, any signal can be approximated as a δ function, occurring once per orbit. The Fourier series representation of a delta function is an infinite sum of sine terms at increasing harmonics. Thus, in the limit

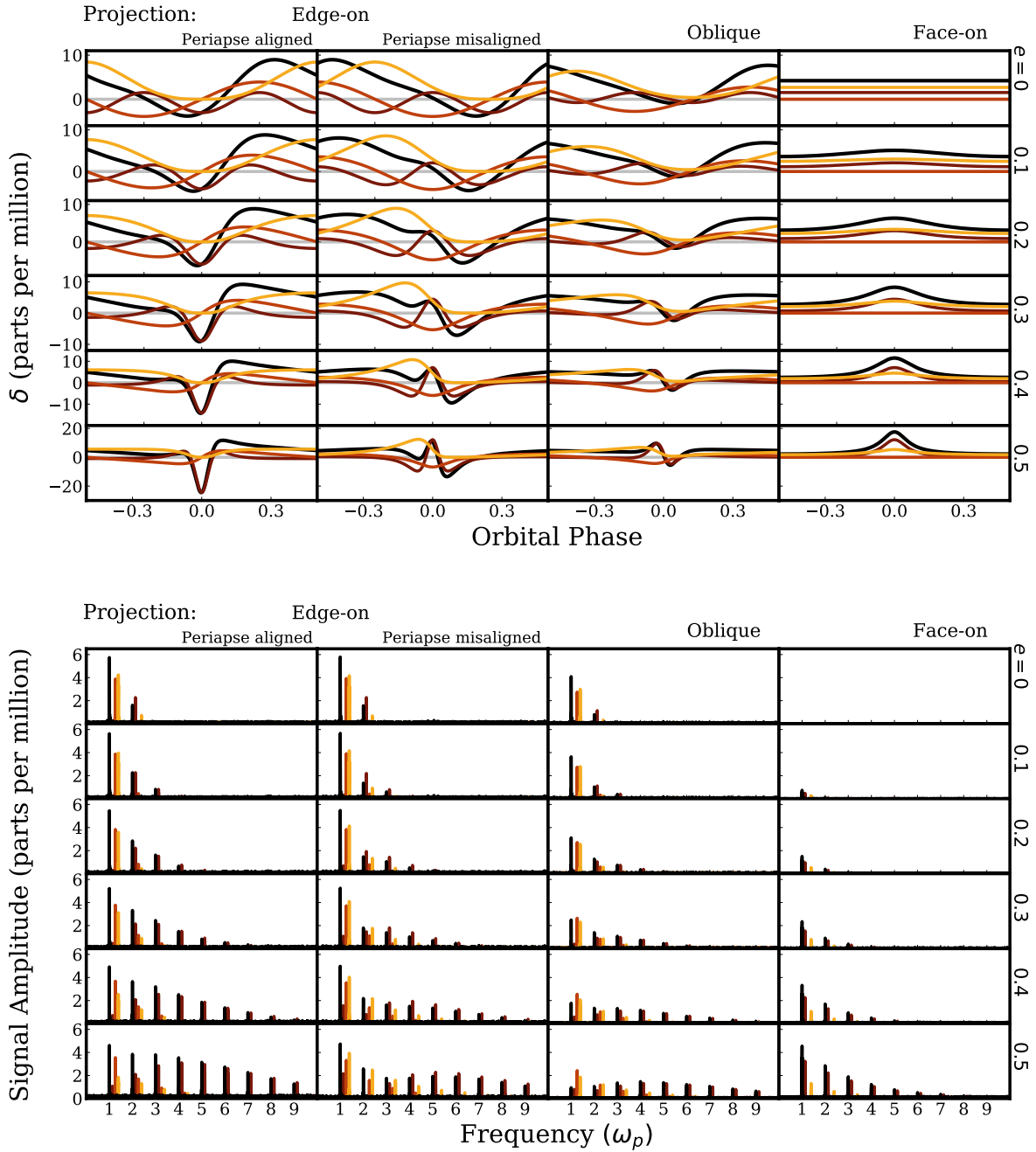


Figure 2. Similar to Figure 1, but shown for a variety of eccentricities and viewing angles (detailed in table 1). We show independently the out-of-transit signal due to tides (dark red), beaming (brick red) and reflections (yellow) as well as the total signal (black). The same system properties, save for the varying eccentricity, are used in each row of subplots. Note that the y-scaling varies between rows in (a). The signal amplitude used in (b) is effectively equal to the coefficients of the Fourier series that can be used to construct $\delta(t)$ (detailed further in the text).

of high eccentricities, the power spectra of each of these signals should tend to having nearly equal power extending up to high harmonics. Indeed this is what we see in Figure 3.

For small eccentricities, we can also derive some intuitive understanding. We can see from Equation 4 that we can express trigonometric functions of η in terms of a Fourier expansion in $e^n \sin(n\omega_p t)$ and $e^n \cos(n\omega_p t)$. Meanwhile, δ depends on powers of η through the time-varying orbital radius (Equation 2) and thus δ can be expressed as an infinite sum of trigonometric functions of $n\omega_p t$. The amplitude of each higher harmonic is reduced by a factor of $\sim e$ compared to the previous harmonic.

4. PROSPECTS FOR DETECTION

We now move to discussion of the prospects and potential difficulties of the detection these higher-order harmonics in real stellar light curves. In particular, we will focus on the Transiting Exoplanet Survey Satellite (TESS, Ricker et al. 2015), which, at the time of writing, is expected to launch imminently.

4.1. Power spectra from TESS

TESS is an all-sky survey which will measure the photometric variation of 200,000 target stars at 2-minute cadence, as well as take full-frame images of its entire 2300 deg^2 field-of-view at 30-minute cadence. Over its two-year primary mission, it will observe azimuthal slices of first the southern and then the northern ecliptic hemisphere, spending ~ 27 days on each slice. Regions of the sky that belong to more than one overlapping slice benefit from a longer observational baseline, with small “continuous-viewing” zones of $\sim 900 \text{ deg}^2$ near the ecliptic poles observed for ~ 351 days each.

TESS is expected to achieve a photometric precision of roughly 50 parts per million. If the period of an observed planetary system can be derived, the data can be folded over that period and binned, reducing the photometric uncertainty by a factor of \sqrt{N} , where N is the number of observed periods. Thus, planets with small semi-major axes, and correspondingly short periods, will be the most promising for detection and characterisation.

Figure 4 shows mock light curves and power spectra for our example planet, given a range of photometric uncertainties and observational baselines. The light curves are sampled at TESS’s 2-minute cadence, with baselines corresponding to the 351, 81, and 27 day-baseline viewing regions of TESS. The simulated uncertainties are Gaussian, using the stated uncertainty in each row of subplots as the width of the distribution.

The 50 parts per million uncertainty row is most relevant to a TESS observation of a system like our example planet. We see that for all but the shortest TESS obser-

vational baseline, the second and third harmonics in the power spectrum are clearly visible, though their relative amplitudes can vary.

Higher photometric precision is obtainable with instruments such as the Hubble Space Telescope (Demory et al. 2015) and the forthcoming James Webb Space Telescope (Beichman et al. 2014), for which errors of order of 10-20 ppm per transit may be attainable. For instruments such as these, an observation of our example system over two periods might be sufficient to resolve the 3rd harmonic and above. The photometric precision of the *Kepler* mission is of order 100 ppm; higher-order harmonics of this example planet would be perfectly observable at this precision over *Kepler*’s four-year observational baseline at *Kepler*’s short observational cadence (~ 1 minute), although this is not shown in Figure 4. As discussed in PS18, many other confirmed exoplanets should also be detectable in archival *Kepler* data.

Our example planet has a characteristic δ of order 10 ppm, but many systems exist for which a significantly larger-amplitude signal would be expected. For larger characteristic δ , the obtainable signal-to-noise ratio increases; for intuition, if the characteristic δ were of order 100 ppm (instead of our example planet’s 10 ppm), the power spectrum plotted in Figure 4 for the 5 ppm error is more representative, in terms of signal-to-noise, of the expected TESS observation. Similarly, shorter-period planets will be much better constrained over the same observational baseline, as more periods can be overlaid.

More rigorous handling of mock observations and the sources of error may alter these results somewhat, and it should be noted that these are intended mostly for illustrative purposes.

4.2. Dependence on system properties

So far, we have focused only on a small slice of the possible parameter space of planetary systems. In PS18, we showed the relative strength of photometric (and spectroscopic) effects for already-confirmed exoplanets, but here we explore the parameter space of possible planetary systems in the abstract.

Figure 5 shows how the maximum δ_t , δ_r , δ_b , and δ_Σ over one planetary orbit differs for various systems.

In each plot, the parameters of our example planet (see Figure 1) are used, save for the one which we vary. This is more physically realistic for some parameters than others: for example, two equivalent planets with very different semi-major axes can exist, but we might be more surprised by two planets with the same mass with markedly different radii. As such, we vary the parameters only over a small (linear) range.

We also only use one projection, the same as in Figure 1, though the results will vary when the system is viewed from other angles.

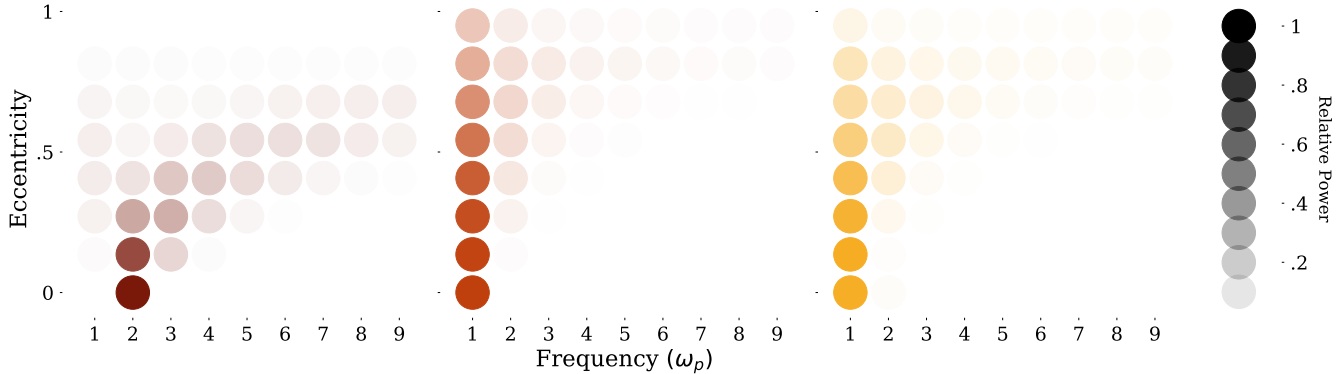


Figure 3. The eccentricity dependence of individual harmonics in the power spectrum, shown individually for tides (dark red), beaming (brick red) and reflections (yellow). The same system parameters are used as in Figure 1 save for varying eccentricity.

We will go through each panel in the order shown, highlighting which signal, if any, dominates in a particular parameter space:

- **Highly eccentric planets** - For a fixed semi-major axis, more eccentric systems have much larger tidal signatures, as tides have the strongest dependence on pericenter distance.
- **Large orbits** - Beaming is dominant for larger orbits (though the amplitude of the signal is small), whilst tides dominate for orbits passing close to the host star.
- **Massive planets** - Both tides and beaming have the same dependence on planetary mass, with larger δ for heavier planets. Reflection signals will dominate for lower masses (this remains true under the assumption of constant planetary density, with $M_p \propto R_p^3$).
- **Giant planets** - Only the reflection signal depends on planetary radius, and thus dominates for larger planets (of fixed mass).
- **Massive stars** - The reflection signal strength is independent of stellar mass, though if we assume constant density (with $M \propto R^3$) the tidal signature is also constant and may dominate. At lower masses, for fixed radii, tides dominate as the outer layers of the star are less gravitationally bound and tidal distortions are larger.
- **Giant stars** - For larger radii, tides dominate, as the distortion of the outer layers becomes larger.

Alternatively, we could ask which regimes of parameter space each signal dominates in:

- **Tides** - Tidal signatures dominate when the outer layers of the star are strongly distorted. This occurs for close orbits and massive planets (where

the pull of the planet is larger) and for large, low-mass stars (where the competing gravity of the star is reduced). Thus tides are promising for examining **eccentric or close-orbiting hot Jupiters, brown dwarfs, or planets around giant stars**. The signals can be very large (up to percentage-level changes in luminosity) and in eccentric systems are visible from all angles.

- **Beaming** - Beaming signals are not very large (at most $\delta_b \sim 10$ ppm for the parameters of these systems), but they are the least dependent on the distance between the planet and the star. Thus they may be of interest in the largest number of systems, though only with sufficient photometric precision. Currently they are of most interest for examining **massive planets on large orbits** (where “large” here still only refers to orbits closer to their star than 1 AU) and planets which are already constrained by **existing radial velocity measurements**.
- **Reflections** - The amount of reflected light is strongly dependent on the planetary radius, and has no direct dependence on the mass of the planet or the star (though assuming planets have uniform density, $\delta_l \propto M_p^{\frac{2}{3}}$) and thus is of most interest in **low-mass or large-radius planets** and **planets around high-mass stars**. Like tides, the signals can be large (up to parts per thousand levels) and for eccentric systems they can be visible from all viewing angles.

5. DISCUSSION AND CONCLUSIONS

In this paper, we have shown that the power spectra of light curves of stars hosting eccentric planets, even at small orbital eccentricities, contain higher-order har-

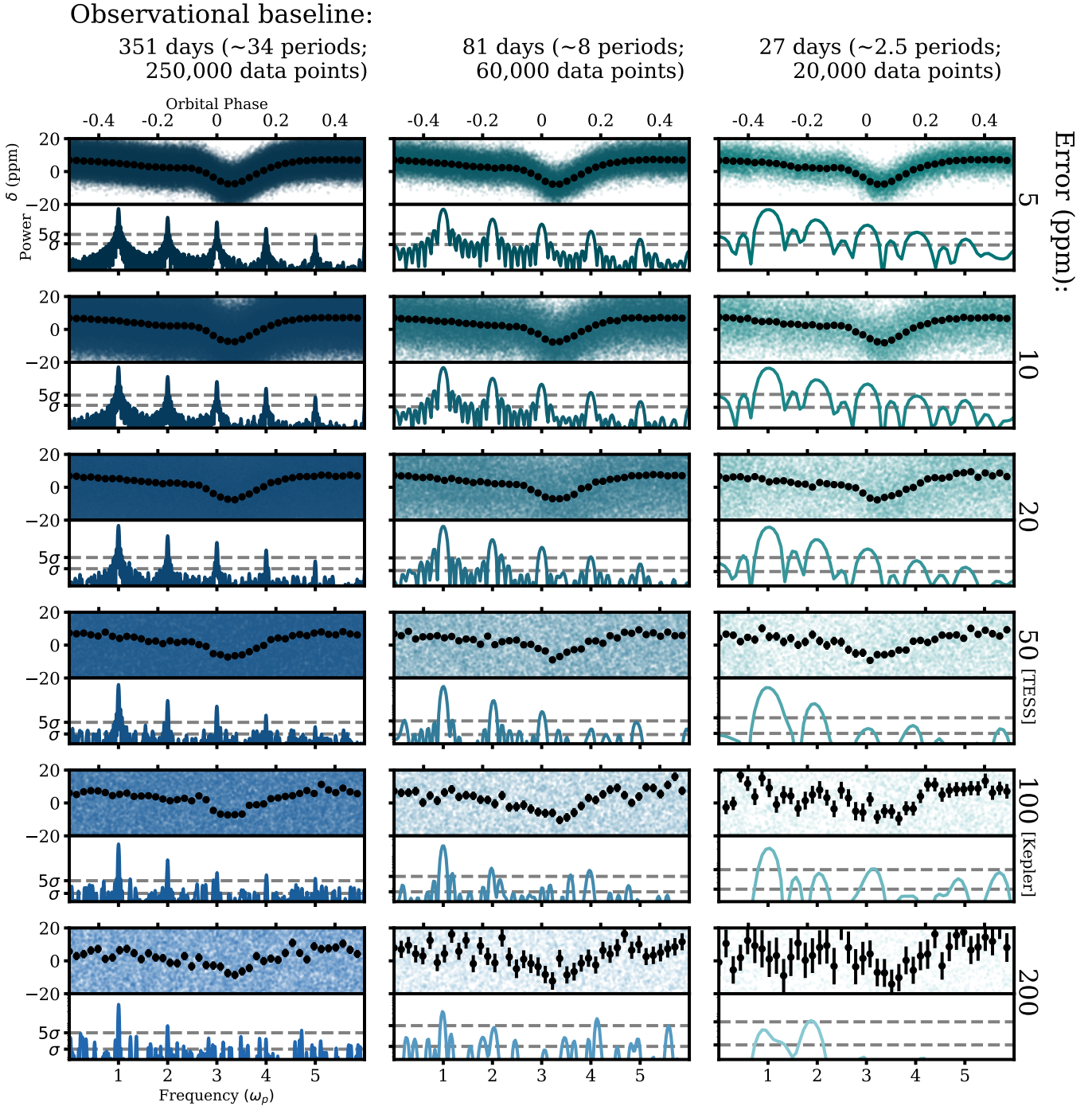


Figure 4. Mock light curves and power spectra for the planetary system of Figure 1, calculated with varying levels of Gaussian-distributed noise over varying observational baselines. Descending rows have higher photometric uncertainty, and columns, moving to the right, have shorter observational baselines. The uncertainty and time sampling is constructed to be directly comparable to the TESS survey (more details in text). Individual data points in the light curve, folded over one period, are shown in colour, and the mean values (averaged over 6-hour bins) are shown in black. The mean and standard deviation of the power spectra are calculated, and the plots show the mean (coinciding with the x-axis) and 1 and 5 standard deviations above this (on a log scale) as dashed gray horizontal lines.

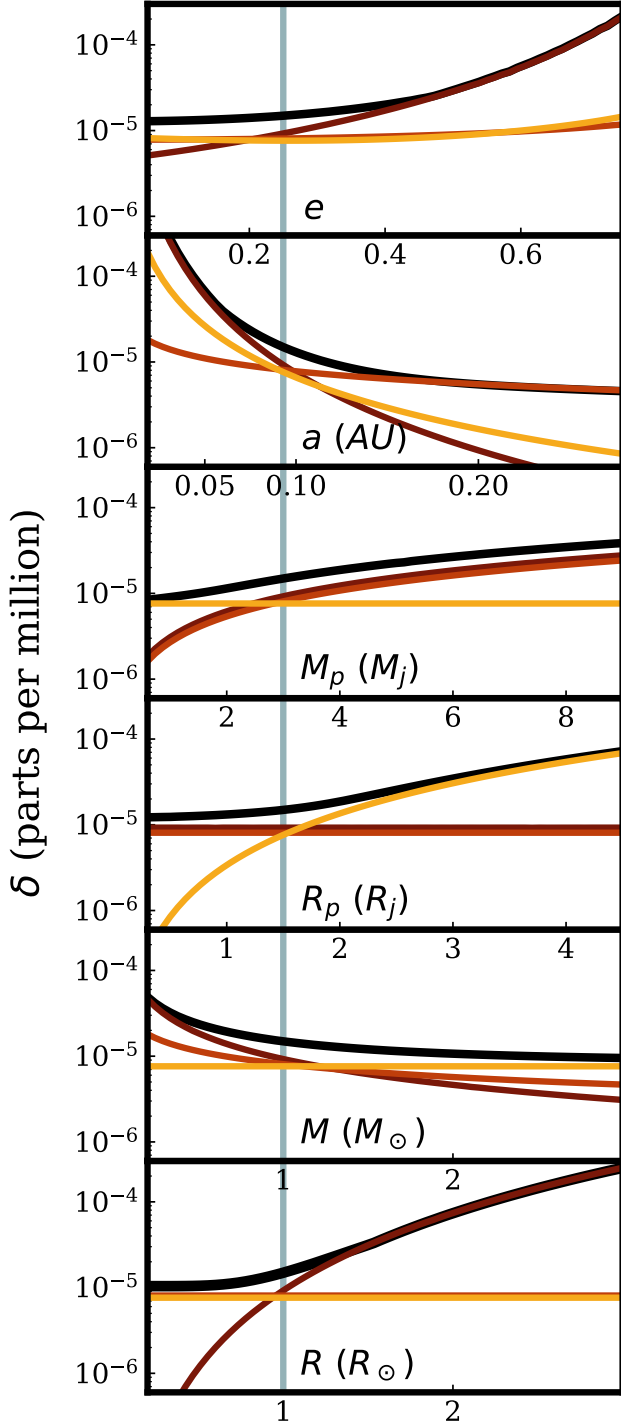


Figure 5. The maximum variation in the light curve due to tides (dark red), beaming (brick red) and reflections (yellow), compared to the total variation (black). The grey line shows the properties of our example planet (as used in Figure 1 and throughout) and the properties of the system are varied independently from these values. All x-scaling is linear and the y-scale is the same for all panels.

monics than can be explained by the assumption of circular orbits.

Variations in the star’s apparent luminosity due to tides, beaming, and/or reflections all give power spectra with peaks at 3 times the planet’s orbital frequency and above. If tides dominate, the spectrum can extend to very high harmonics, and the dominant frequency may itself be a high harmonic.

In Section 4, we show that these effects will be visible in surveys such as TESS and *Kepler* for many known planets, and that more will be detectable in both existing and future data. As shown in PS18, eccentric planets should be visible regardless of viewing angle for systems with strong reflection or tidal signals.

We also discuss the strength of these three signals across the possible parameter space for systems hosting exoplanets. We show that tides will give the largest possible signals, especially for eccentric hot-Jupiters and giant stars. Reflections will dominate for lower-mass planets, whilst beaming is of most interest for planets on larger orbits (though the signal will be small).

We provide public code, *OoT*, for calculating the photometric effect of tides, beaming, and reflections as a function of time and the system properties. This is detailed in Appendix A.

5.1. Using power spectra as a tool for planet detection

Here, we have highlighted observable effects in the power spectrum due to the photometric signals of tides, beaming, and reflection, each of which depends differently upon the parameters of the planetary system in question. Consequently, we might hope to use power spectra to characterise planetary systems. However, this is considerably beyond the scope of the present work.

Simple diagnostics are possible when the power spectrum is both well-resolved and dominated by a single signal of the three, or when the parameters of the system are very well constrained by independent observations.

However, in most systems, there will be significant degeneracies between the contributions to the power spectrum of different out-of-transit signals. Measurement error will further complicate any attempt to fit data to predicted power spectra. In short, power spectra are not an independently useful tool for characterising planets. It will be fitting models to the light curve, not the power spectrum, that will yield tight constraints on system properties.

In spite of the difficulty of using power spectra to characterise planets, power spectra are by far the most useful and easily accessible tool for *finding* planets (or at least hinting at their existence). Power spectra are relatively easy to produce for any light curve, as they require no foreknowledge of the system, and preserve only the periodic photometric signals present in the light curve.

Most out-of-transit signals are low-amplitude, and likely very difficult to observe in the light curve over a single period. It is only when data are stacked over many planetary periods that the signal becomes clear and models can be fitted. But this requires knowledge of the presence of a planet, and of its period. This is the invaluable information that the power spectrum tells us.

Where once planets were detected through a single clear signal, such as a transit, we are now entering an era where signs of the same system can be observed via many different methods. The out-of-transit effects discussed here are small, but they are universal. They depend heavily on multiple parameters of the system, which makes them complex to model, but also breaks

degeneracies and tells us about myriad aspects of the planet, star, and orbit.

Particularly as we seek to stretch not just the number, but the range of known planets and their properties, we will have to leverage small-amplitude signals and the combined effect of many independent observations and physical processes. The power spectrum is simply one, though will often be the first, of the tools needed to do this.

ACKNOWLEDGEMENTS

We thank Nicholas C. Stone, Adam Wheeler, Alex Teachey, Tiffany Jansen, and David Kipping for their helpful comments and discussions.

APPENDIX

A. THE OOT PACKAGE

Alongside this paper, we present a public python code, `OoT` (short for *Out-of-Transit*), for calculating light curves and radial velocity profiles for planetary systems without transits.

The light curves are calculated using equations 10, 15 and 16, and they thus include the effects of tides, beaming and reflections. Radial velocity profiles include the effects of orbital motion and tides (see PS18, equations 74 and 77).

Though we focus on out-of-transit effects, all calculations are valid for all orientations, including those in which the planet eclipses the star. If a user wishes to model a transit as well, they can use the `BATMAN` package (Kreidberg 2015). `OoT` contains a function which will convert the parameters of the system to those required by `BATMAN` (with the exception of the limb darkening parameters).

The user also has the option to model secondary eclipses are also modelled. A Lambert sphere, when seen from the direction of illumination, is uniform in surface brightness (the full moon is an excellent example of this). Thus we calculate the area of the planet blocked by the star at any given time (which is simply the area of intersection of two circles), and we have an excellent approximation to the effects of the star eclipsing the planet.

The system properties which must be supplied, and their units, are detailed in table A1.

As the equations governing out-of-transit behaviours are simple and analytic, the calculation is very efficient. The only bottleneck comes from the numerical solution of η as a function of t (from equation 4). We apply an efficient and accurate approximation to make this directly calculable: Let η_0 satisfy

$$\eta_0 = \sqrt{\frac{a^3}{GM}}t. \quad (\text{A1})$$

Now assume $\eta = \eta_0 + \eta_1$ where $\eta_1 \ll \eta_0$. We can substitute this back into equation 4 and subtract all terms involving t to give

$$\eta_1 = e \sin(\eta_0 + \eta_1) = e \sin \eta_0 + O(e^2). \quad (\text{A2})$$

One can repeat the same exercise to find the second- and third-order components (and indeed we could go to infinity but we show some restraint here) to give

$$\eta = \eta_0 + \eta_1 + \eta_2 + \eta_3 + O(e^4) \quad (\text{A3})$$

where

$$\eta_2 = e^2 \sin \eta_0 \cos \eta_0 \quad (\text{A4})$$

and

$$\eta_3 = e^3 \sin \eta_0 \left(1 - \frac{3 \sin^2 \eta_0}{2}\right). \quad (\text{A5})$$

Thus $\eta(t)$ can be found directly to sufficient accuracy, meaning all formulae necessary for calculating out-of-transit behaviour can be computed effectively instantaneously. Indeed, input times can be given to `OoT` as an array and the calculation is vectorised, thus the computational cost should not scale. It is also possible to revert back to the exact solution, although this is significantly slower.

Parameter	Default Unit
M - stellar mass	M_{\odot}
M_p - planet mass	M_{\odot} ($\approx 1000M_j$)
R - stellar radius	R_{\odot}
R_p - planet radius	R_{\odot} ($\approx 10R_j$)
a - semi-major axis	R_{\odot} ($\approx 0.005AU$)
e - eccentricity	unitless
A_g - geometric albedo	unitless
β - stellar response to tides	unitless
θ_v - polar viewing angle	radians
ϕ_v - azimuthal viewing angle	radians
t_p - time at periape	days

Table A1. The parameters used by the `0oT` package to calculate light curves, radial velocity profiles and photometric power spectra. All orbital parameters refer to the planet. Though the user can vary A_g and β , throughout this paper we have used assumed values (0.15 and 1 respectively).

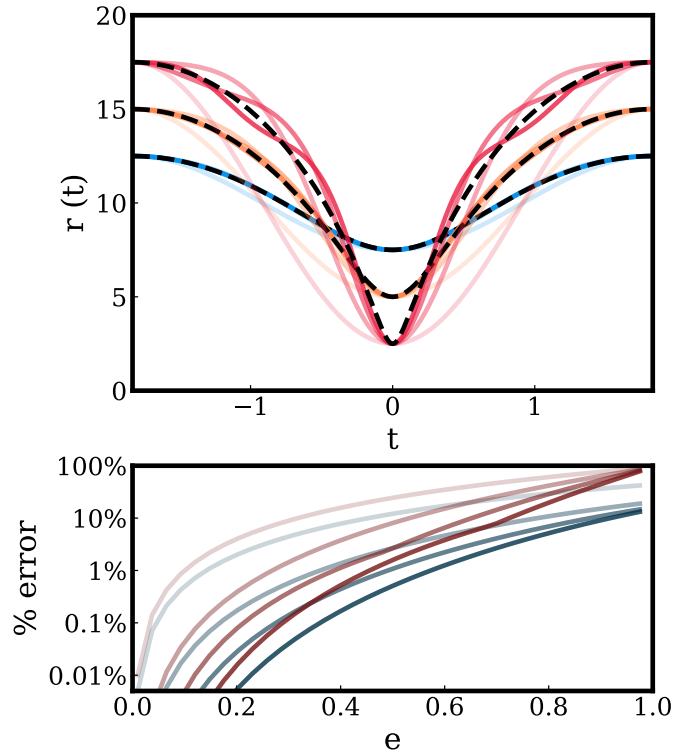


Figure A1. Upper panel: Exact orbital radius (dashed black line) compared to the approximate solutions accurate to increasing powers of e (darker lines). The orbits shown have $e = 0.25$ (blue), $e = 0.5$ (orange) and $e = 0.75$ (red). Lower panel: The maximum (dark red) and time averaged (dark blue) fractional error in the radius derived from our approximate solution over one period. Darker lines show higher orders of the approximation.

Figure A1 shows the accuracy of this approximation over one orbital period for a range of eccentricities. It can be seen that it is generally a good fit, though less so for very high e , and that the largest error comes from the approximate solution dawdling too long near periape. Note that although our most accurate solution only contains terms $\propto e^3$, the radius depends on η only through a term $e \cos \eta$ and thus the radius is accurate up to terms of order approximately e^6 .

The code is written entirely in units of days, M_{\odot} , and R_{\odot} , save for velocities, which are always returned in ms^{-1} . We have included functionality to convert units to years, seconds, Jupiter- and Earth-radii and masses (for R_p and M_p), and astronomical units (for a).

REFERENCES

- Armstrong, C., & Rein, H. 2015, *MNRAS*, 453, L98
- Batygin, K., Bodenheimer, P. H., & Laughlin, G. P. 2016, *ApJ*, 829, 114
- Beichman, C., Benneke, B., Knutson, H., et al. 2014, *ArXiv e-prints*, arXiv:1411.1754
- Binney, J., & Tremaine, S. 2008, *Galactic Dynamics: Second Edition* (Princeton University Press)
- Charbonneau, D., Brown, T. M., Latham, D. W., & Mayor, M. 2000, *ApJL*, 529, L45
- Charbonneau, D., Noyes, R. W., Korzennik, S. G., et al. 1999, *ApJL*, 522, L145
- Cowan, N. B., & Agol, E. 2011, *ApJ*, 729, 54
- Cowan, N. B., Chayes, V., Bouffard, É., Meynig, M., & Haggard, H. M. 2017, *MNRAS*, 467, 747
- Demory, B.-O., Ehrenreich, D., Queloz, D., et al. 2015, *MNRAS*, 450, 2043
- Esteves, L. J., De Mooij, E. J. W., & Jayawardhana, R. 2013, *ApJ*, 772, 51
- Henry, G. W., Marcy, G., Butler, R. P., & Vogt, S. S. 1999, *IAUC*, 7307
- Jansen, T., & Kipping, D. 2017, *ArXiv e-prints*, arXiv:1710.10213
- Kane, S. R., Ciardi, D. R., Gelino, D. M., & von Braun, K. 2012, *MNRAS*, 425, 757
- Kreidberg, L. 2015, *PASP*, 127, 1161
- Lin, D. N. C., Bodenheimer, P., & Richardson, D. C. 1996, *Nature*, 380, 606
- Loeb, A., & Gaudi, B. S. 2003, *ApJL*, 588, L117
- Lovis, C., & Fischer, D. 2010, *Radial Velocity Techniques for Exoplanets*, ed. S. Seager, 27–53
- Matsumura, S., Takeda, G., & Rasio, F. A. 2008, *ApJL*, 686, L29
- Morris, S. L. 1985, *ApJ*, 295, 143
- Naoz, S., Farr, W. M., Lithwick, Y., Rasio, F. A., & Teyssandier, J. 2011, *Nature*, 473, 187
- Penoyre, Z., & Stone, N. C. 2018, *ArXiv e-prints*, arXiv:1803.05917
- Press, W. H., & Rybicki, G. B. 1989, *ApJ*, 338, 277
- Ricker, G. R., Winn, J. N., Vanderspek, R., et al. 2015, *Journal of Astronomical Telescopes, Instruments, and Systems*, 1, 014003
- Seager, S. 2010, *Exoplanet Atmospheres: Physical Processes*
- Seager, S., & Mallén-Ornelas, G. 2003, *ApJ*, 585, 1038
- TriAUD, A. H. M. J., Collier Cameron, A., Queloz, D., et al. 2010, *A&A*, 524, A25
- VanderPlas, J. T. 2017, *ArXiv e-prints*, arXiv:1703.09824
- Winn, J. N., & Fabrycky, D. C. 2015, *ARA&A*, 53, 409